Decoupled and Analytic Model of the Quad-Active-Bridge DC/DC Converter under Transmitting Instantaneous Pulsating Power

Xin Peng[1], Yonglei Zhang[1], Jianliang Pan[1], Yuhuan Qin[1], Yan Li[1], Saeed Jahdi[2] and Xibo Yuan[1]
[1]School of Electrical Engineering, China University of Mining and Technology, Xuzhou, China
[2]School of Electrical, Electronic and Mechanical Engineering, University of Bristol, Bristol, United Kingdom

Abstract—**The quad-active-bridge (QAB) DC/DC converter has shown superior advantages in eliminating the low-frequency voltage ripple in the cascaded wind power converter. However, the power flowing into the QAB converter contain low-frequency pulsation, causing low-frequency envelope oscillation issues inside the QAB converter. This paper proposes a decoupled and analytic model for quantitively analyzing the corresponding operation characteristics. Specifically, a summation difference transformation is proposed to decouple the multivariable coupling model as a diagonal decoupled model. The QAB converter voltages with time-varying angles are decomposed as the supervision of multiple frequency components by the Bessel function. Various characteristics such as input current stress (peak and rms), low-frequency envelope oscillations have been thoroughly analyzed under instantaneous pulsating power transmission with the proposed model. These results can be further used for designing more high-performance control strategies to optimize operation. Simulation and experimental results are presented to validate the proposed analytic model.**

***Index Terms*—Cascaded wind power converters with quad-active-bridge DC/DC converters, decoupled and analytic model, instantaneous pulsating power transmission, summation difference transformation and Bessel function.**

I. Introduction

With the increasing power rating of a single wind turbine towards 20MW and the increasing distance of the offshore wind power generation systems [1], higher voltage levels (lower current amplitude) and higher reliability (lower maintenance cost) configurations will be more preferred.

At present, the three-level neutral-point clamped (NPC) converters are widely used in offshore wind power systems. The voltage of the NPC converter can cover 1140V, 3.3kV or 4.16kV levels. The power of a three-level NPC converter can cover 2MW to 8MW by using different power devices such as IGBTs, paralleled IGBTs or IGCTs [2]. In theory, by connecting multiple NPC converter units, the power level can be further extended to 20MW. However, the voltage level of the three-level NPC converter can be further increased hardly due to the limitation of its own structure. The control strategy is more complicated and the reliability decreases with the increasing NPC converter units. Hence, various novel wind power converters are proposed for future 20MW offshore wind power systems [3].

Fig. 1 shows a modified high-power cascaded wind power converter for offshore wind power systems [4-5]. Fig. 1(a) is the overall structure. As seen, the generator is connected to the cascaded power modules where the generator voltage can be improved constantly, up to 10kV. The output of each power module is connected to a grid-side inverter. Multiple inverters running in parallel are connected to the grid through a step-up transformer. Fig. 1(b) shows the structure of a single power module. The generator-side rectifier is composed of three single-phase H-bridge cells. The quad-active-bridge (QAB) DC/DC converter is connected with both the generator-side rectifier and the grid-side inverter. The instantaneous pulsating power from the generator-side rectifier is converged by the QAB converter. The low-frequency pulsating power (three-phase angle different 240°) inside the instantaneous power is eliminated. Hence, there is no need to install many high-voltage capacitors, which are poor power density and reliability [6]. The modified cascaded wind power converter can satisfy both the higher voltage and the higher reliability requirements.

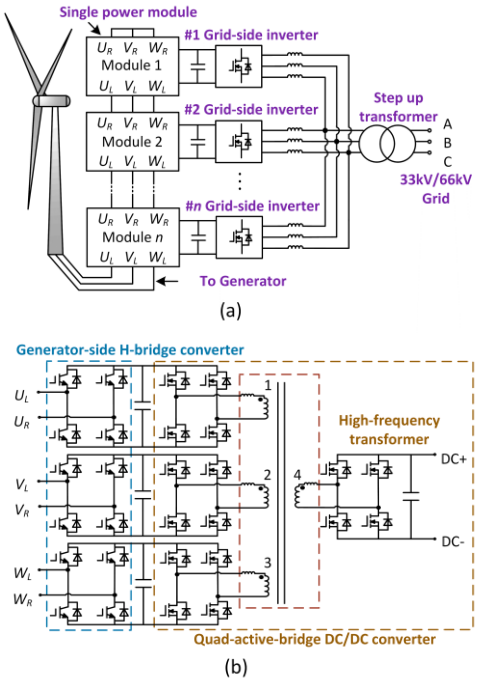

Fig. 1. Wind power generation systems using a modified cascaded converter with quad-active-bridge converters [4]. (a) The overall structure. (b) Single power module.

It should be noted that the instantaneous pulsating power flowing into the QAB converter consists of two parts: *i.e.* the DC active power and the low-frequency pulsating power (twice of the frequency of the generator stator (f_0)) [7]. The superposition of these two kinds of power will introduce a low-frequency envelope oscillation phenomenon in the three high-frequency H-bridge cells (connected to the generator-side rectifier, shown in Fig. 1(b)) and the corresponding transformer windings. As shown in Fig. 2, when the QAB converter transmits the pulsating power, the coordinate operating characteristics are quite different from that of the only DC active power. These low-frequency oscillations will increase the current stress (peak and rms) and the losses of the QAB converter. Hence, a decoupled and analytic model of the QAB converter is needed to evaluate these characteristics quantitively.

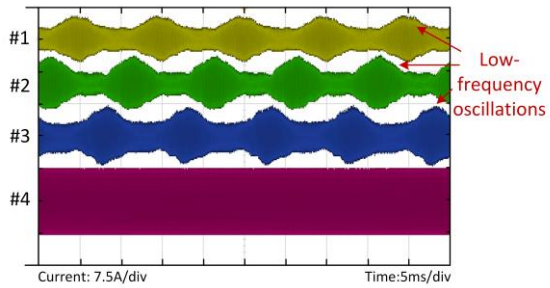

Fig. 2. Experimental results of the QAB converter currents.

Generally, when the phase-shifted angles of DC/DC converters are kept almost unchanged, the small-signal modelling method [8] is adopted. When transmitting instantaneous pulsating power, the phase-shifted angles of the high-frequency transformer voltages are constantly change, causing complex nonlinear coupling between transformer voltages and currents. In this condition, the working characteristics of the QAB converter should be derived by a large-signal model.

Various large-signal modelling methods have been presented in the literature [9-14] for the model of DC/DC converters. These modelling methods can be mainly grouped into the discrete modelling methods [9-10] and the continuous modelling methods [11-14]. The discrete modelling methods can obtain high-precision solutions, while the computational process is quite complex. The continuous modelling methods can be further divided into the ones using the state equation [11-12] or the equivalent circuit [13-14]. For example, the Generalized State Space Averaging (GSSA) method [11] uses the state equation to describe the switching circuit operating under diverse conditions and then expands the state variable by Fourier decomposition. However, due to the differential equations of the state equation, solving the specific analytical formulas becomes challenging. The large-signal model can also be established by the equivalent circuit with the First Harmonic Approximation (FHA) method [14], where the converter is converted into its equivalent circuit, and the square wave voltage is substituted with its fundamental wave. However, the error of the established model is quite large.

The QAB converter operates in a high-frequency switching state for transmitting pulsating power. This operating mode is quite like the frequency modulation (FM) technique in communication applications [15], where the modulation frequency changes with the amplitude of the transmitted signals. The Bessel function is usually used to decompose the nonlinear FM combination waveforms [16], which can be adopted to eliminate the non-linear coupling caused by the time-varying phase-shifted angles.

In this article, to quantitively analyze the operating characteristics of the QAB converter with instantaneous pulsating power transmission, a decoupled and analytic model is proposed. First, a multivariable nonlinear coupling matrix model is established by the QAB converter equivalent circuit, where the square wave voltage is substituted with its fundamental wave and low-order harmonics by the Fourier decomposition to reduce error. Next, utilizing the summation difference matrix transformation, the above nonlinear coupling equivalent circuit matrix is decoupled as a diagonal matrix. Hence, the currents transmitting different powers (DC active power or low-frequency pulsating power) can be separated. Meanwhile, to figure out the input current stress (peak and rms), the waveforms with different frequencies coupled together obtained by the above Fourier decomposition are completely decoupled by the Bessel function. With the proposed model, the operating characteristics of the QAB converter with instantaneous pulsating power transmission can be analytically and quantitively derived, and the following conclusions can be obtained:

1) The low-frequency envelope oscillations are only caused by the transmitted low-frequency pulsating power, and can be decreased with the pulsation decreasing.

2) The peak and rms of each input current are magnified by 2 and 1.2247(*sqrt*(6)/2) times separately due to the instantaneous pulsating power.

These findings can reflect the inner characteristics of the QAB converter under instantaneous pulsating power transmission, and can be further used to modify the control strategies to optimize the converter operation.

The rest of this article is organized as follows: In Section II, the principle of the instantaneous pulsating power transmission is given. In Section III, a decoupled and analytic model and corresponding operating characteristics are presented. In Section IV, simulation and experimental results are provided to validate the above analysis. Finally, Section V concludes this article.

II. The Principle of the Instantaneous Pulsating Power Transmission

In this section, the principle of the instantaneous pulsating power transmission is briefly introduced.

For each power module, the instantaneous pulsating power ($p_{U\sim W}(t)$) of the three-phase H-bridge rectifier at the generator-side can be derived as shown in (1). As can be seen, each phase contains the DC active power and the low-frequency pulsating power, where the frequency is twice of the frequency of the generator stator (f_0).

$$\begin{cases} p_U(t) = \dfrac{U_S I_S}{2}\cos\varphi + \dfrac{U_S I_S}{2}\cos(2\omega_0 t - \varphi) \\ p_V(t) = \dfrac{U_S I_S}{2}\cos\varphi + \dfrac{U_S I_S}{2}\cos(2\omega_0 t - \varphi - \dfrac{4\pi}{3}) \\ p_W(t) = \dfrac{U_S I_S}{2}\cos\varphi + \dfrac{U_S I_S}{2}\cos(2\omega_0 t - \varphi + \dfrac{4\pi}{3}) \end{cases} \quad (1)$$

Where U_S and I_S respectively represent the amplitude of the output voltage and current, ω_0 is the angular velocity of the generator stator, and φ is the power factor angle of the generator.

In addition, the difference of the phase angles of the three-phase low-frequency pulsating power is 4π/3, if adding the three-phase instantaneous power together, the low-frequency pulsating power part can be effectively eliminated as zero as shown in Fig. 3.

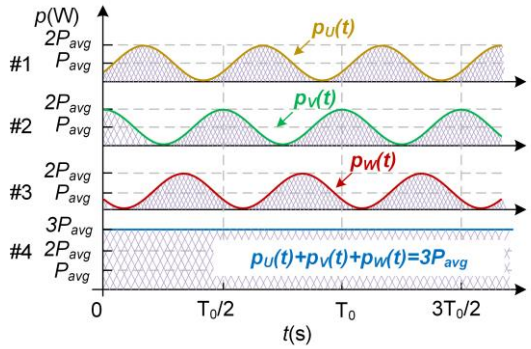

Fig. 3. The process of the three-phase instantaneous pulsating power aggregation in the QAB converter.

Fig. 4 shows the control and modulation strategies of the QAB DC/DC converter. Among, Fig. 4(a) shows the control diagram of the QAB converter. To realize the above objective, the proportional integral resonance (PIR) controller [4] is used to provide an enough large gain at the frequency of $2\omega_0$. The output of the PIR controller is the phase-shifted angle. The phase-shifted angle of the 4th H-bridge connected to the grid-side inverter is fixed, and the phase-shifted angles of the primary-side three H-bridges connected to the generator-side rectifier are controlled as different, as shown in (2).

$$\begin{cases} d_{1\wedge4} = (m_1\cos\varphi + m_2\cos(2\omega_0 t - \varphi)) \\ d_{2\wedge4} = (m_1\cos\varphi + m_2\cos(2\omega_0 t - \varphi - \dfrac{4\pi}{3})) \\ d_{3\wedge4} = (m_1\cos\varphi + m_2\cos(2\omega_0 t - \varphi + \dfrac{4\pi}{3})) \end{cases} \quad (2)$$

Where, m_1 and m_2 respectively represent the phase-shifted angle amplitude of the transmitted DC active power and low-frequency pulsating power. Fig. 4(b) shows the modulation strategy of the QAB DC/DC converter. To simplify the modulation strategy, when transmitting instantaneous pulsating power, the QAB converter remain employs the general single-phase-shift (SPS) modulation.

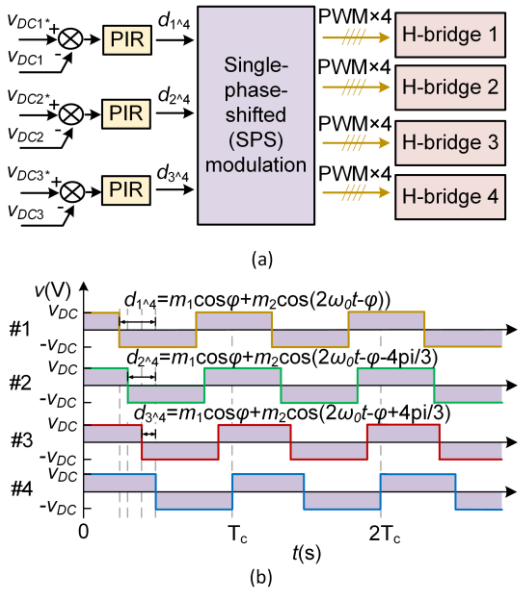

Fig. 4. The control and modulation strategies. (a) Input voltage closed-loop control. (b) Single-phase-shift modulation.

III. The Proposed Decoupled and Analytic Model

In this section, a multivariable decoupled and analytic matrix model is established by a proposed summation difference coordinate transformation method and the Bessel function decomposition method.

A. Multivariable matrix coupling model

Fig. 5 shows the equivalent circuit of the QAB converter. Where, $v_1(t)$~$v_4(t)$ respectively represent the input and output voltages. Z_L is the leakage impedance parameter of #1-3. Z_4 is the leakage impedance parameter of #4. According to the equivalent circuit, the leakage impedance currents $i_1(t)$~$i_4(t)$ can be expressed as (3).

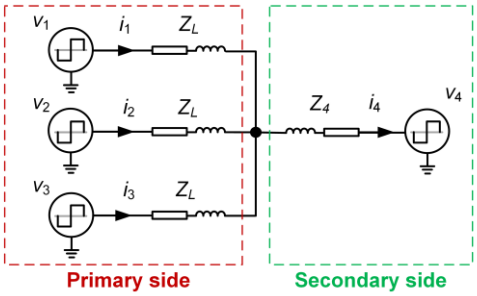

Fig. 5. The equivalent circuit of the QAB DC/DC converter.

$$\begin{cases} i_1(t) = \dfrac{(2Z_4 + Z_L) * v_1(t) - Z_4 * v_2(t) - Z_4 * v_3(t) - Z_L * v_4(t)}{Z_L(3Z_4 + Z_L)} \\ i_2(t) = \dfrac{(2Z_4 + Z_L) * v_2(t) - Z_4 * v_1(t) - Z_4 * v_3(t) - Z_L * v_4(t)}{Z_L(3Z_4 + Z_L)} \\ i_3(t) = \dfrac{(2Z_4 + Z_L) * v_3(t) - Z_4 * v_1(t) - Z_4 * v_2(t) - Z_L * v_4(t)}{Z_L(3Z_4 + Z_L)} \\ i_4(t) = i_1(t) + i_2(t) + i_3(t) \end{cases} \quad (3)$$

The above equations can be formulated as an admittance matrix model as shown in (4). Since this is a non-diagonal matrix, there are complex coupling interactions between multiple ports. Generally, the above coupling can be decoupled by the Thevenin theorem, whereas, the corresponding decoupled process is quite complicated.

$$\begin{bmatrix} i_1(t) \\ i_2(t) \\ i_3(t) \end{bmatrix} = \begin{bmatrix} Y_1 & -Y_2 & -Y_2 \\ -Y_2 & Y_1 & -Y_2 \\ -Y_2 & -Y_2 & Y_1 \end{bmatrix} * \begin{bmatrix} v_1(t)-v_4(t) \\ v_2(t)-v_4(t) \\ v_3(t)-v_4(t) \end{bmatrix} \quad (4)$$

$$Y_1 = \frac{2Z_4 + Z_L}{Z_L(3Z_4 + Z_L)} \qquad Y_2 = \frac{Z_4}{Z_L(3Z_4 + Z_L)}$$

In addition, considering the operation principle of the QAB converter, the converter voltages (v_1~v_4) are square waves. If directly using the Fourier analysis method to decompose these voltages, the following equation shown in (5) and (6) can be derived. As seen, the voltage v_4 can be easily decomposed as multiple signals with fixed frequencies. However, the voltage (v_1~v_3) will be decomposed as multiple signals with unfixed frequencies, caused by the phase-shifted angles $d_{i\wedge4}$. One important challenge, the above method will generate the interaction between multiple signals with unfixed and time-varying frequency signals, causing non-linear couplings.

$$\begin{cases} v_i(t) = \dfrac{4V_{DC}}{\pi} \begin{Bmatrix} \sin(\omega_c t - d_i\pi) \\ +1/3\sin[3(\omega_c t - d_i\pi)] + \cdots \\ +1/n\sin[n(\omega_c t - d_i\pi)] \end{Bmatrix} \\ i = 1,2,3 \end{cases} \quad (5)$$

$$v_4(t) = \frac{4V_{DC}}{\pi} \begin{Bmatrix} \sin\omega_c t + 1/3\sin(3\omega_c t) \\ +1/5\sin(5\omega_c t) + \cdots + 1/n\sin(n\omega_c t) \end{Bmatrix} \quad (6)$$

where, V_{DC} represents the voltage value of the DC bus, and the four DC link voltages of the QAB converter are the same. ω_c is the angular velocity of the power devices.

By substituting (5) and (6) into the model in (4), the equivalent system model of the QAB converter can be obtained. However, the model cannot be used to analyze the operating characteristics of the QAB converters quantitatively, which can be decoupled by the following proposed method.

B. Summation difference coordinate transformation method

In this part, the complex admittance circuit matrix is decoupled by the summation difference transformation. The summation difference matrix (T_{SD}) is shown in (7).

$$T_{SD} = \begin{bmatrix} 1 & 1 & 1 & 1 \\ 1 & -1 & 0 & 0 \\ \vdots & \cdots & \ddots & \vdots \\ 1 & 0 & \cdots & -1 \end{bmatrix} \quad (7)$$

Pre-multiply (4) by (7), a new diagonal matrix model can be derived in the summation difference coordinate, as shown in (8). In (8), the input currents are transformed as the summation current (i_{sum}) and the difference currents ($i_{1\wedge2}$, $i_{1\wedge3}$). The voltages ($v_{1\text{-}3}$) are transformed as the summation voltage (v_{sum}) and the difference voltages ($v_{1\wedge2}$, $v_{1\wedge3}$). With the above transformation, the non-diagonal coupling matrix model can be transformed as a diagonal matrix, meaning the summation current is only controlled by the summation voltage, the difference currents are only controlled by the difference voltages.

$$\begin{cases} \begin{bmatrix} i_{sum}(t) \\ i_{1\wedge2}(t) \\ i_{1\wedge3}(t) \end{bmatrix} = \begin{bmatrix} Y_{sum} & 0 & 0 \\ 0 & Y_{dif} & 0 \\ 0 & 0 & Y_{dif} \end{bmatrix} * \begin{bmatrix} v_{sum}(t) - 3v_4(t) \\ v_1(t) - v_2(t) \\ v_1(t) - v_3(t) \end{bmatrix} \\ Y_{sum} = \dfrac{1}{3Z_4 + Z_L} \quad Y_{dif} = \dfrac{1}{Z_L} \quad v_{sum}(t) = v_1(t) + v_2(t) + v_3(t) \\ i_{sum}(t) = i_1(t) + i_2(t) + i_3(t) \quad i_{1\wedge2}(t) = i_1(t) - i_2(t) \\ i_{1\wedge3}(t) = i_1(t) - i_3(t) \end{cases} \quad (8)$$

For the summation voltage part that does not contain the coupling between the voltage with unfixed frequency signals, the available small-signal modelling method can be directly utilized. Only the phase-shifted angles of the difference voltages are time-varying, the difference currents cannot easily be solved.

C. Proposed Bessel function decompose method

In (5), each decomposed sinusoidal wave by Fourier decomposition contains a constant change of the phase-shifted angle (d_i). Such sinusoidal formulas are commonly employed in frequency modulation (FM) of wireless communication. Generally, In FM, the sinusoidal formula can be effectively decoupled by the Bessel function, as illustrated in (9).

$$\begin{cases} \cos(m\sin\omega_0 t) = J_0(m) + 2J_2(m)\cos 2\omega_0 t + \cdots \\ \sin(m\sin\omega_0 t) = 2J_1(m)\sin\omega_0 t + 2J_3(m)\sin 3\omega_0 t + \cdots \end{cases} \quad (9)$$

where, $J_n(x)$ is the parameter of each simplified wave by the Bessel function. The parameter value $J_n(x)$ of each simplified wave by the Bessel function is shown in Fig. 6.

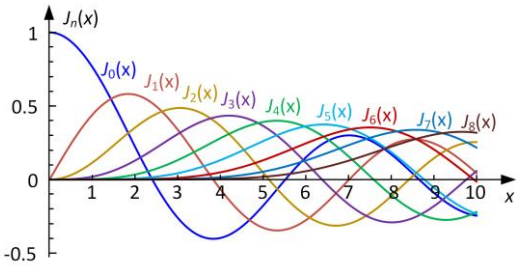

Fig. 6. The coefficient ($J_n(x)$) value of the Bessel function.

To achieve a thorough decoupling of the sinusoidal formulas in (5), it is necessary to convert the sinusoidal formulas in (5) into the standard formula as shown in (9). This article takes the input voltage v_1 as an example, input voltages v_2 and v_3 exhibit similarities with that of v_1, albeit with a phase difference of 240°. The resulting conversion for v_1 is presented in (10).

$$\begin{cases} v_1(t)=\dfrac{4V_{DC}}{\pi}\begin{Bmatrix}\sin\{\omega_c t-d_{1*}\pi\}\\ +1/3\sin\{3[\omega_c t-d_{1*}\pi]\}\\ +\cdots+1/j\sin\{j[\omega_c t-d_{1*}\pi]\}\end{Bmatrix} \\ d_1=m_1\cos\varphi+m_2\sin(2\omega_0 t+\varphi_t) \\ \varphi_t=\dfrac{\pi}{2}-\varphi \quad j=1,3,\cdots,2n-1 \end{cases} \tag{10}$$

Hence, employing the Bessel function, the input voltage v_1 can be completely decomposed as (11).

$$\begin{cases} v_1(t)=\dfrac{4V_{DC}}{\pi}\sum_{j=1}^{2n-1}\dfrac{1}{j}f_{1,j}(t) \qquad j=1,3,5,\cdots,2n-1 \\ f_{1,j}(t)=g_{1,j,0}(t)+\sum_{i=1}^{n}g_{1,j,i}(t) \\ g_{1,j,0}(t)=J_0(jm_2\pi)\sin[j\omega_c t-jm_1\pi\cos\varphi] \\ g_{1,j,i}(t)=(-1)^i J_i(jm_2\pi)\sin[(j\omega_c+2i\omega_0)t-(jm_1\pi\cos\varphi \\ -i\varphi_t)]+J_i(jm_2\pi)\sin[(j\omega_c-2i\omega_0)t-(jm_1\pi\cos\varphi+i\varphi_t)] \end{cases} \tag{11}$$

With the above decomposition, the QAB converter voltage v_1 has been transformed as multiple signals with fixed frequencies, where the frequencies are $j\omega_c \pm 2i\omega_0$ (j=1,3,5, … ,2n-1, i=0,1,2,3, …, n). The multivariable coupling matrix model is also transformed into a decoupled linear diagonal matrix model. With this proposed decoupled and analytic model, the input current i_1 can be expressed with formulas, as shown in appendix.

D. Math and Equations

Utilizing the above proposed decoupled and analytic model, the operation characteristics of the QAB DC/DC converter under transmitting instantaneous pulsating power can be obtained.

After transforming back to the n-dimensional by analyzing the current with different powers, the peak of the QAB converter input currents can be expressed as:

$$\begin{cases} i_{1\text{peak}}(t)=\dfrac{V_{DC}m_2}{2f_c L}\cos(2\omega_0 t-\varphi)+\dfrac{V_{DC}m_1}{2f_c(L+3L_4)}\cos\varphi \\ i_{2\text{peak}}(t)=\dfrac{V_{DC}m_2}{2f_c L}\cos(2\omega_0 t-\varphi-\dfrac{4\pi}{3})+\dfrac{V_{DC}m_1}{2f_c(L+3L_4)}\cos\varphi \\ i_{3\text{peak}}(t)=\dfrac{V_{DC}m_2}{2f_c L}\cos(2\omega_0 t-\varphi+\dfrac{4\pi}{3})+\dfrac{V_{DC}m_1}{2f_c(L+3L_4)}\cos\varphi \end{cases} \tag{12}$$

Where, each input current amplitude ($i_{\text{peak}}(t)$) is influenced by the DC link voltage (V_{DC}), switching frequency (f_c), leakage inductance (L, L_4), power factor (cosφ), and the coefficient of the phase-shifted angle (m_1, m_2). When the QAB converter is used to transmit instantaneous pulsating power, the amplitude of each input current will increase by one times than only transmitting the DC active power. Moreover, the low-frequency envelope oscillations are only related to the transmitted low-frequency pulsation. The low-frequency envelope oscillation can decrease as the low-frequency pulsation decreasing.

The rms of the QAB converter input current can be expressed in (13).

$$\begin{cases} I_{\text{rms\_}DC}=\dfrac{\sqrt{3(3-2m_1)}}{3}\dfrac{V_{DC}m_1}{2f_c(L+3L_4)}\cos\varphi \\ I_{\text{rms\_}ALL}=\dfrac{\sqrt{6}}{2}I_{\text{rms\_}DC} \end{cases} \tag{13}$$

Where, $I_{\text{rms\_DC}}$ is the rms of the QAB converter input current under only transmitting the DC active power. $I_{\text{rms\_DC}}$ is influenced by the DC link voltage (V_{DC}), switching frequency (f_c), leakage inductance (L, L_4), power factor (cosφ), and the coefficient of the phase-shifted angle (m_1). When the QAB converter is used to transmit instantaneous power, the rms of the overall current($I_{\text{rms\_}ALL}$) will be increased by 1.2247 (*sqrt*(6)/2) times than that of transmitting the DC active power.

IV. Simulation and Experimental Results

A. Simulation Results

To validate the accuracy of the proposed decoupled and analytic model of the QAB converter under transmitting instantaneous pulsating power, the current waveforms of the QAB converter are calculated by utilizing MATLAB/Simulink with the same parameters of the experimental prototype shown in TABLE I.

TABLE I
PARAMETERS OF EXPERIMENTAL PROTOTYPE

Symbol	Description	Value
P	Rate DC power (kW)	2
f_0	AC frequency (Hz)	50
$u_{\text{DC1-4}}$	Port voltage (V)	300
f_s	Switching frequency (Hz)	50k
L	Primary side leakage inductance (μH)	32.8
L_4	Secondary side leakage inductance (μH)	50.3
k	Ratio of transformer	1:1:1:1

Fig. 7 shows the simulation waveforms of the input and output voltages (v_1, v_4) with instantaneous pulsating power transmission. As can be seen, the voltages (v_1, v_4) calculated by the decoupled and analytic model are the same with the ideal voltages (v_{1*}, v_{4*}).

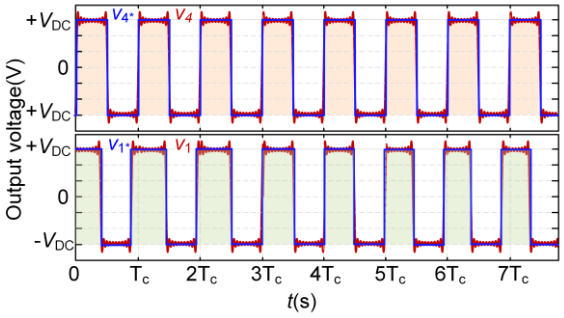

Fig. 7. The waveforms of the simulated voltage (v_1, v_4) and the ideal voltage (v_{1*}, v_{4*}) with instantaneous power transmission.

Fig. 8 shows the simulation waveforms of the decoupled currents and the QAB converter current i_1 with

instantaneous pulsating power transmission. As can be seen, the decoupled currents consist of the difference currents ($i_{1\wedge2}$, $i_{1\wedge3}$) transmitted low-frequency pulsating power between the primary side and the summation current (i_{1DC}) transmitted DC active power from the primary to the secondary side. The measured amplitude of i_{1DC} and i_1 are 2.5A and 5A respectively, which are consistent with the calculated results by formula (12). Meanwhile, the rms of i_{1DC} and i_1 are 2.34A and 2.86A respectively, which are consistent with the calculated results by formula (13).

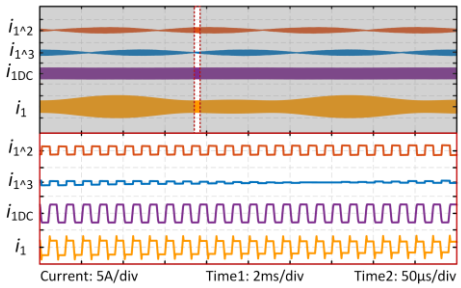

Fig. 8. The simulation waveforms of the decoupled input current i_1.

To sum up, the theoretical analysis of the proposed decoupled and analytic model can be proved by the above simulation results.

B. *Experimental Results*

A low-power experimental prototype is built for verifying the proposed decoupled and analytic model of the QAB converter under transmitting instantaneous pulsating power, as shown in Fig. 9. The generator-side converter is built by the IPM module (PM50RL120). The QAB converter use silicon carbide devices for working at high frequency, as shown in Fig. 9(b). Fig. 9(c) is the picture four-winding high-frequency transformer. The leakage inductance of this transformer is relatively small, extra inductors are also added to provide enough inductance for transmitting power.

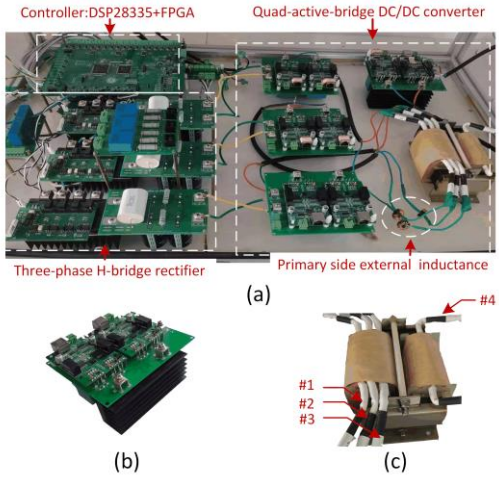

Fig. 9. The downscaled experimental prototype: (a) The overall structure of a single power module. (b) The SiC MOSFET H-bridge unit. (c) The four-winding high-frequency transformer.

Fig. 10 shows the QAB DC/DC converter primary-side input voltages ($v_{1\text{-}3}$) by a 10s persistence mode. As can be seen, the phase-shifted angle of each input voltage is time-varying under transmitting instantaneous pulsating power. Fig. 11 shows the DC link voltage($v_{DC1\text{-}3}$) of the generator-side rectifier, where the amplitude and frequency of the generator-side rectifier input current (i_A) is varying. As can be seen, the voltage ripple of each DC link of the generator-side rectifier can be eliminated and is not affected by the varying input current.

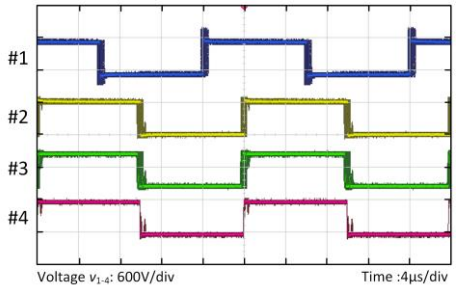

Fig. 10. The experimental waveforms of the QAB converter voltage $v_{1\text{-}4}$ under persistence mode.

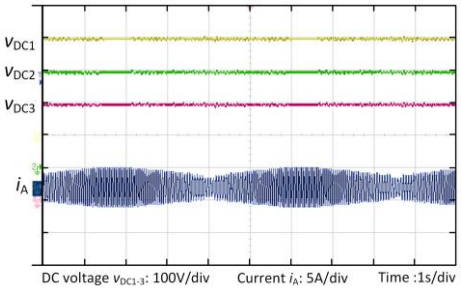

Fig. 11. The experimental results of the generator-side DC bus voltage with the generator-side rectifier input current varying.

The above results prove that the QAB converter can effectively eliminate the low-frequency voltage ripple of the DC bus, and is stable and reliable.

Fig. 12 shows the input current i_1 and output current i_4 of the QAB converter with changing instantaneous pulsating power. As seen, with the increase of the transmitted overall power from 1.5kW to 2kW, the input current amplitude i_{1peak} is also increased from 3.24A to 4.91A. Moreover, the calculated results by (12) are almost the same with that of the measured, which can further validate the correctness of the proposed decoupled and analytic model.

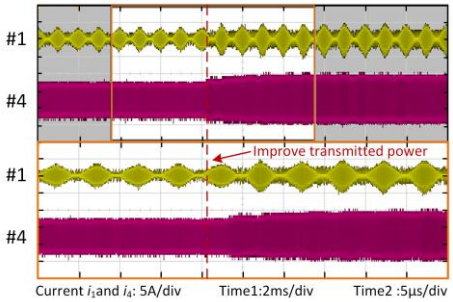

Fig. 12. The experimental results of the input current i_1 and output current i_4 with increasing instantaneous pulsating power.

Fig. 13 shows the input current i_1 with changing low-frequency pulsating power. As can be seen, with the

decrease of the transmitted low-frequency pulsating power, the low-frequency envelope oscillations of the input current are also decreased. The results prove that the low-frequency envelope oscillations can be decreased with the transmitted low-frequency pulsation decreasing.

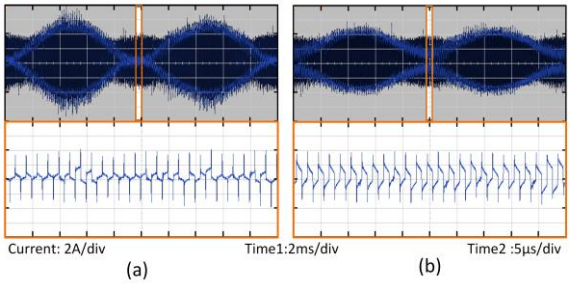

Fig. 13. The experimental current i_1 with decreasing the transmitted low-frequency pulsation: (a) All the low-frequency pulsation. (b) Decrease the low-frequency pulsation.

To sum up, the above experiment results can prove the correctness of the operating characteristics obtained by the proposed decoupled and analytic model.

V. Conclusions

This paper presents a new decoupled and analytic model for building a linear and diagonal (decoupled) matrix model for the QAB DC/DC converter with instantaneous pulsating power transmission. With the proposed summation difference coordinate transformation method, the power transmitting into the QAB converter can be separated as the DC active power and the low-frequency pulsating power, both of which can be analyzed separately. The Bessel function in communication applications is introduced to decompose the QAB converter voltage with time-varying phase-shifted angles. The rms values of each input current will be magnified by 1.2247 (*sqrt*(6)/2) times. The input current peak will be also doubled. The low-frequency envelope oscillations can be decreased with the transmitted low-frequency pulsating power decreasing.

With the proposed decoupled and analytic model, the operation characteristics of the QAB converter with instantaneous pulsating power transmission can be revealed, which can provide guidelines for exploring more high-performance control strategies.

Acknowledgment

This work was supported in part by the National Natural Science Foundation of China under grant no.52107218.

References

[1] Y. Fu, Y. Liu, L. Huang, F. Ying and F. Li, "Collection system topology for deep-sea offshore wind farms considering wind characteristics," *IEEE Trans. Energy Convers*., vol. 37, no. 1, pp. 631-642, March. 2022.

[2] Medium voltage wind converter, ABB wind turbine converters, PCS6000, full power converter, up to 12MW, https://new.abb.com/power-converters-inverters/wind-turbines/utility-scale/pcs6000.

[3] X. Yuan, Y. Zhang and X. Peng, "Power converter technologies for 20MW wind turbines," *in IEEE ECCE 2022 Conf.*, pp. 1-8, Oct. 2022.

[4] Y. Zhang, X. Peng, X. Yuan, Y. Li and K. Wang, "A unidirectional cascaded high-power wind converter with reduced number of active devices," *IEEE Access*., vol. 11, pp. 10902-10911, 2023.

[5] Y. Zhang, P. Zhu, X. Yuan, X. Peng, Y. Li, X. Wu. "Low-capacitance high-power cascaded wind turbine system with instantaneous power convergence and transition," *Power Syst. Technol*., vol.46, no. 7, pp. 2759- 2767, Jul. 2022.

[6] Y. Pan, J. Teng, C. Yang, Z. Bu, B. Wang, X. Li and X. Sun., "Capacitance minimization and constraint of CHB power electronic transformer based on switching synchronization hybrid phase-shift modulation method of high frequency link," *IEEE Trans. Power Electron*., vol. 38, no. 5, pp. 6224-6242, May. 2023.

[7] X. Li, L. Cheng, L. He, Z. Zhu, Y. Yang and C. Wang, "Capacitor voltage ripple minimization of a modular three-phase AC/DC power electronics transformer with four-winding power channel," *IEEE Access*., vol. 8, pp. 119594-119608, 2020.

[8] G. Zheng, C. Qi, Y. Liu, J. Liang, H. Wang and M. Fu, "Uniform and simplified small-signal model for inductive power transfer systems," *IEEE Trans. Power Electron.*, vol. 38, no. 2, pp. 2709-2719, Feb. 2023.

[9] G. Gao, W. Lei, Q. Tang, Z. Xiao, X. Hu and Y. Wang, "Decomposed discrete-time model and multiscale oscillations analysis of the DAB converter," *IEEE Trans. Power Electron*., vol. 35, no. 9, pp. 9133-9150, Sept. 2020.

[10] S. Shao, L. Chen, Z. Shan, F. Gao, H. Chen, D. Sha, T. Dragičević, "Modeling and advanced control of Dual-Active-Bridge DC–DC converters: a review," *IEEE Trans. Power Electron*., vol. 37, no. 2, pp. 1524-1547, Feb. 2022.

[11] P. Azer and A. Emadi, "Generalized state space average model for multi-phase interleaved Buck, Boost and Buck-Boost DC-DC converters: transient, steady-state and switching dynamics," *IEEE Access*., vol. 8, pp. 77735-77745, 2020.

[12] H. Qin and J. W. Kimball, "Generalized average modeling of Dual Active Bridge DC–DC converter," *IEEE Trans. Indust. Electron*., vol. 27, no. 4, pp. 2078-2084, April. 2012.

[13] A. Sankar, A. Mallik and A. Khaligh, "Extended harmonics based phase tracking for synchronous rectification in CLLC converters," *IEEE Trans. Indust. Electron*., vol. 66, no. 8, pp. 6592-6603, Aug. 2019.

[14] E. S. Glitz, J. -D. Hsu and M. Ordonez, "Power loss estimation in LLC synchronous rectification using rectifier current equations," *IEEE Trans. Indust. Electron*., vol. 67, no. 5, pp. 3696-3704, May. 2020.

[15] X. Yang, K. Ding and G. He, "Accurate separation of amplitude-modulation and phase-modulation signal and its application to gear fault diagnosis," *J. sound vibr*., vol 452, pp.34-50, Jul. 2019.

[16] D. G. Kurup and A. Koithyar, "New expansions of Bessel functions of first kind and complex argument," *IEEE Trans. Antennas Propag*., vol. 61, no. 5, pp. 2708-2713, May. 2013.

APPENDIX

$$i_1(t)=\frac{1}{3}[Y_{\text{sum}}*(v_{\text{sum}}(t)-3v_4(t))+Y_{\text{dif}}*(3v_1(t)-v_{\text{sum}}(t))] \tag{14}$$

$$Y_{\text{sum}}*v_{\text{sum}}(t)=\frac{12V_{DC}}{\pi}\sum_{j=1}^{2n-1}\{[Y_{\text{sum}}*g_{1,j,0}(t)+Y_{\text{sum}}*g_{1,j,3}(t)+\cdots+Y_{\text{sum}}*g_{1,j,i}(t)] \qquad n=1,3,6,\cdots\} \tag{15}$$

$$Y_{\text{sum}}*g_{1,j,0}(t)=\left\{\frac{J_0(jm\pi)}{\sqrt{R^2+[\omega_{\text{c}}(L+3L_4)]^2}}\sin(j\omega_{\text{c}}t-jm\pi\cos\varphi-\arctan\frac{\omega_{\text{c}}(L+3L_4)}{R}) \qquad j=1,3,,\cdots,2n-1\right\} \tag{16}$$

$$Y_{\text{sum}}*g_{1,j,n}(t)=\left\{\begin{array}{l}(-1)^n\dfrac{J_n(jm\pi)}{\sqrt{R^2+[(j\omega_{\text{c}}+2n\omega_0)(L+3L_4)]^2}}\sin[(j\omega_{\text{c}}+2n\omega_0)t-(jm\pi\cos\varphi-n\varphi_t)\\ -\arctan\dfrac{(j\omega_{\text{c}}+2n\omega_0)(L+3L_4)}{R}]+\dfrac{J_n(jm\pi)}{\sqrt{R^2+[(j\omega_{\text{c}}-2n\omega_0)(L+3L_4)]^2}}\sin[(j\omega_{\text{c}}-2n\omega_0)t\\ -(jm\pi\cos\varphi+n\varphi_t)-\arctan\dfrac{(j\omega_{\text{c}}-2n\omega_0)(L+3L_4)}{R}]\end{array}\right\} \tag{17}$$

$$Y_{\text{sum}}*v_4(t)=\frac{J_j(0)}{\sqrt{R^2+[j\omega_{\text{c}}(L+3L_4)]^2}}\sin(j\omega_{\text{c}}t-\arctan\frac{j\omega_{\text{c}}(L+3L_4)}{R}) \tag{18}$$

$$Y_{\text{dif}}*v_1(t)=\frac{4V_{DC}}{\pi}\left\{\begin{array}{l}\dfrac{J_0(jm\pi)}{\sqrt{R^2+(j\omega L)^2}}\sin(j\omega_{\text{c}}t-jm\pi\cos\varphi-\arctan\dfrac{j\omega_{\text{c}}L}{R})+(-1)^n\dfrac{J_n(jm\pi)}{\sqrt{R^2+[(j\omega_{\text{c}}+2n\omega_0)L]^2}}\sin[(j\omega_{\text{c}}\\ +2n\omega_0)t-(jm\pi\cos\varphi-n\varphi_t)-\arctan\dfrac{(j\omega_{\text{c}}+2n\omega_0)L}{R}]+\dfrac{J_n(jm\pi)}{\sqrt{R^2+[(j\omega_{\text{c}}-2n\omega_0)L]^2}}\sin[(j\omega_{\text{c}}\\ -2n\omega_0)t-(jm\pi\cos\varphi+n\varphi_t)-\arctan\dfrac{(j\omega_{\text{c}}-2n\omega_0)L}{R}]\end{array}\right\} \tag{19}$$

$$\left\{\begin{array}{l}Y_{\text{dif}}*v_{\text{sum}}(t)=\dfrac{12V_{DC}}{\pi}\sum_{j=1}^{2n-1}\{[Y_{\text{dif}}*g_{1,j,0}(t)+Y_{\text{sdif}}*g_{1,j,3}(t)+\cdots+Y_{\text{dif}}*g_{1,j,i}(t)] \qquad n=1,3,6,\cdots\}\\ Y_{\text{dif}}*g_{1,j,0}(t)=\left\{\dfrac{J_0(jm\pi)}{\sqrt{R^2+(\omega_{\text{c}}L)^2}}\sin(j\omega t-jm\pi\cos\varphi-\arctan\dfrac{\omega_{\text{c}}L}{R}) \qquad j=1,3,5,\cdots,2n-1\right\}\\ Y_{\text{dif}}*g_{1,j,n}(t)=\left\{\begin{array}{l}(-1)^n\dfrac{J_n(jm\pi)}{\sqrt{R^2+[(j\omega_{\text{c}}+2n\omega_0)L]^2}}\sin[(j\omega_{\text{c}}+2n\omega_0)t-(jm\pi\cos\varphi-n\varphi_t)-\arctan\dfrac{(j\omega_{\text{c}}+2n\omega_0)L}{R}]\\ +\dfrac{J_n(jm\pi)}{\sqrt{R^2+[(j\omega_{\text{c}}-2n\omega_0)L]^2}}\sin[(j\omega_{\text{c}}-2n\omega_0)t-(jm\pi\cos\varphi+n\varphi_t)-\arctan\dfrac{(j\omega_{\text{c}}+2n\omega_0)L}{R}]\end{array}\right.\end{array}\right. \tag{20}$$